FRONT MATTER

Title

Towards Adaptive Robotic Sampling of Phytoplankton in the Coastal Ocean

Authors

Trygve O. Fossum[*,1,10], Glaucia M. Fragoso[2], Emlyn J. Davies[4], Jenny E. Ullgren [7], Renato Mendes [5,6], Geir Johnsen[2,8,10], Ingrid Ellingsen[4], Jo Eidsvik[3], Martin Ludvigsen[1,8,10] and Kanna Rajan[5,9,10].

Affiliations

[*]Corresponding Author: *trygve.o.fossum@ntnu.no*
[1]Department of Marine Technology,
Norwegian University of Science and Technology (NTNU), Trondheim, Norway.
[2]Department of Biology, NTNU, Trondheim, Norway.
[3]Department of Mathematical Sciences, NTNU, Trondheim, Norway.
[4]SINTEF Ocean AS, Trondheim, Norway.
[5]Underwater Systems and Technology Laboratory, Faculty of Engineering,
University of Porto, Portugal.
[6]CESAM, Department of Physics, University of Aveiro, Aveiro, Portugal.
[7]Runde Environmental Centre, Runde, Norway.
[8]University Centre in Svalbard (UNIS), Longyearbyen, Norway.
[9]Department of Engineering Cybernetics, NTNU, Trondheim, Norway.
[10]Centre for Autonomous Marine Operations and Systems (AMOS), Trondheim, Norway.

Abstract

Currents, wind, bathymetry, and freshwater run-off are some of the factors that make coastal waters heterogeneous and patchy, and an environment of scientific interest, where it is challenging to resolve the spatio-temporal variation within the water-column. We present methods and results from field experiments using an autonomous underwater vehicle (AUV) with embedded

algorithms that focus sampling on features in 3-dimensions (3D). This is achieved by combining Gaussian Process (GP) modeling with onboard robotic autonomy allowing volumetric measurements to be made at fine scales. Special focus is given to the patchiness of phytoplankton biomass, measured as Chlorophyll *a* (Chla), an important factor for understanding biogeochemical processes in the coastal ocean, such as primary productivity. During multiple field tests in Runde, Norway, the method was successfully used to identify, map, and track the sub-surface Chlorophyll *a* maxima (SCM). Results show that the algorithm was able to estimate the SCM volumetrically, enabling the AUV to track the maximum concentration depth within the volume. This data was subsequently verified and supplemented with remote sensing, time-series from a buoy, and ship-based measurements from a fast repetition rate fluorometer (FRRf), particle imaging systems, as well as discrete water samples, covering both the large and small scales of the microbial community shaped by coastal dynamics. By bringing together diverse methods from statistics, autonomous control, imaging, and oceanography, the work showcases an interdisciplinary perspective in robotic observation of our changing oceans.

Summary

Autonomous tracking and mapping of phytoplankton biomass in 3D using Gaussian process models embedded on an AUV.

Introduction

Processes controlling the growth and accumulation of phytoplankton are central to nutrient, carbon, and energy cycling; these provide the foundations for the marine and human food web (*1, 2*). Despite their ubiquitous presence across the upper water-column in the global ocean, phytoplankton presents a remarkable heterogeneity in spatial distribution (we will refer to this heterogeneity as patchiness) which is observable in micro-scale (sub centimeter, (*3*)), kilometer scale (*4*), and up to more than 600 km (*5*). Sampling in such a wide range of spatial scales is both challenging and interesting, since patchiness has been shown to strongly influence ecosystem stability (*6*), diversity (*7*), and productivity (*8*). Furthermore, measuring phytoplankton is complicated as observations are based on the proxy measurement of peak absorption of light at 675 nm, originating from photosynthetic Chlorophyll *a* (Chla) inside planktonic cells.

With the growing capability of robotic vehicles, adaptive coverage of the water-column is increasingly viable even if it continues to be challenging to operate in the harsh confines of the water-column and the dynamic coastal ocean. Motivated by this, this work describes the use of propelled robotic platforms, known as autonomous underwater vehicles (AUVs), for optimizing mapping of water-column features in three dimensions. Such *volumetric surveys* of the water-column are of substantial scientific interest as they provide better insight for understanding and

measuring factors such as primary productivity, a vital indicator for the health of our oceans.

To do so, we concentrate on volumetric sampling of *sub-surface chlorophyll maxima* (SCM) using adaptive sampling methods. In particular, the goal is to develop adaptive behavior for AUVs that can enable increased sampling resolution of water-column processes in 3-dimensions (3D) by focusing sampling efforts in regions of interest. In order to do so, an important simplification is done: namely, limiting the survey to a bounding box with a certain size, introducing both a spatial and temporal constraint, similar to the *enclosure citerion* used in (*9*). Shortening the survey time means that the temporal effects will be minimal, and the error contributions from currents, navigation drift, and other time-dependent effects will be bounded allowing complex time variability to be mitigated. This then transforms into a purely spatial problem of finding the relevant sampling locations within the surveyed volume, given a scientific context (for our case the maximum Chla concentration depths). Assuming that only limited prior information is available, obtaining an *a priori* estimate of the SCM feature has significant benefits, contrary to conducting an adaptive survey directly using interior (inside the 3D volume) measurements. This direct approach is ineffective due to two main reasons. First, the AUV will have no forward looking data to guide adaptation, resulting in a coverage that is subject to a "hit-or-miss" trade-off. Given the limited volume of the survey, the adaptation distance available for such an approach is not present. Second, a key driver is the need to survey the most interesting aspects of the feature as fast and accurately as possible to reduce time-dependent effects. Building up an accurate estimate of the interior will be central to achieving this goal, as both the probability of losing track of the feature and survey time can be reduced.

The method suggested in this work is designed to adhere to these ideas by separating the survey into a dedicated exploration and exploitation phase as follows: The AUV first starts by covering the sides of the bounding box volume in an initial phase dubbed `MODE1`, followed by an adaptive survey of the interior volume, dubbed `MODE 2`, capitalizing on the learned information captured in a *Gaussian process* (GP) model, during `MODE 1` (full details are given in the Materials and Methods section). Thus, the exploitation phase is a single calculated maneuver based on the available information, allowing the AUV to survey a region of interest in the water-column in a fast and focused manner, towards attaining a quasi-synoptic snapshot of the feature.

Our experiments were conducted in Runde, Norway, in June 2017 (see Fig. 1) with the algorithm embedded on an AUV to detect and map the SCM, providing a 3D map of the Chla concentration, denoted as [Chla].Note that we specifically define concentration with [Chla]. This is different from "(Chla)", which is an abbreviation for Chlorophyll *a*. The measurements were complemented with photo-physiological data derived from a Fast Repetition Rate fluorometer (FRRf), and two particle imaging systems (SINTEF `SilCam`) (*10*) with different magnifications. These were profiled from a winch, together with a CTD (conductivity, temperature, and depth) sensor and water samples taken from the research vessel *R/V Gunnerus* at stations around Runde. An overview of the involved systems, scales, and platforms is given in Fig. S.2.

In-situ measurements of the size, concentration and type of particulate material in the water-column is critical in order to resolve spatial distributions of the particles in question, while minimizing disruption to them (*11*). A wide range of techniques could be used for such measurements: optical backscatter, fluorescence, laser diffraction (*12*), digital holography (*13*), and telecentric transmittance imaging (*10, 14*), each providing specific information about suspended particulate material. However, it is not possible for a single instrument to obtain measurements of the entire size range of suspended material present in natural seawater, making it necessary to combine multiple techniques in order to monitor the full range of size and types. By combining measurements, a detailed picture of the water column can be rendered with both biometric and volumetric information; providing fine detail for resolving the *in-situ* features while reducing errors related to aliasing and patchiness.

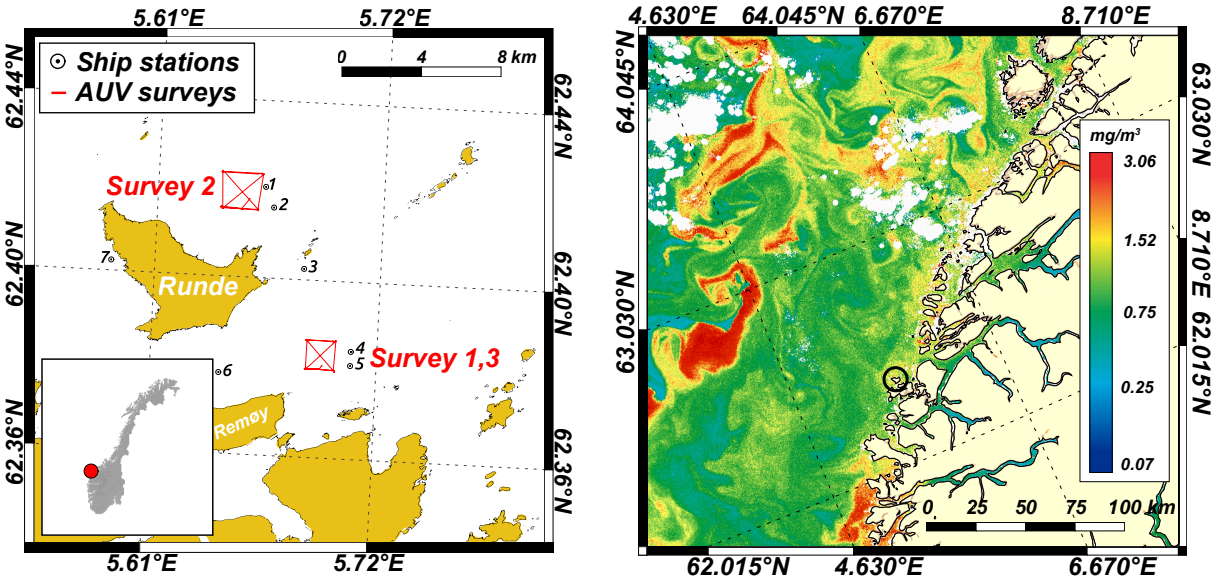

(a) Experiment sampling stations and AUV surveys.

(b) Sentinel 3 image of Chla concentration.

Figure 1: (a) shows the map of the operational area with the three AUV surveys indicated (Survey 1 and 3 [South East of Runde], and Survey 2 [North of Runde]), while the ship-based sampling stations are denoted by numbers (stations 1-7). In the lower corner a small map of Norway is shown with Runde marked in red. (b) shows the Chla (OC4ME) product from OLCI (Ocean and Land Colour Instrument), a multispectral medium resolution instrument on-board ESA's Sentinel-3. The image from 2^{nd} of May is showing the Chla patchiness in the coastal zone, some months prior to the surveys. Runde is shown encircled in black. ©ESA CC BY-SA IGO 3.0.

Related Work

Tracking and sampling biomass distributions using autonomous platforms, is still in its infancy. However, methodological studies are regularly reported and several experiments have been conducted in the recent past. (*15*) introduced AUV-based sampling for eco-physiological work. Focusing on harmful algal blooms (HABs), (*16*) combined AUV surveys with remote sensing towards attaining 3D information about bloom conditions. Similarly (*17*) used a long endurance AUV to sample the peak-Chla layer along horizontal cross-sections for HAB monitoring using onboard gene processing equipment. (*18*) used Hidden Markov Models to enable online estimation of water-column properties, enabling water samples to be triggered under certain upwelling conditions in the Monterey Bay. The same region was explored in (*9*), where a GPS-tracked Lagrangian drifter was used in combination with AUVs for coordinated sampling of dynamic oceanic features, trying to follow the sides of a volume of water as it moved with sub-surface currents. More decision-based efforts in sampling are presented in (*19*), where GPs are used in an online optimal choice approach to adaptively decide where to trigger water samples in the water-column based on biomass concentration. In (*20*), cooperative tracking of phytoplankton blooms using buoyancy driven gliders driven by ocean model predictions is articulated. This was developed further in (*21*), where the sampling resolution was modified by adjusting the undulation angle of a glider, while accounting for ocean currents, with the aim to characterize and sample blooms. (*22*) Discusses problems related to estimating spatio-temporal correlation in time-varying fields and compares Euclidean and Lagrangian approaches using AUV and drifter information to perform spatial interpolation. Feature tracking of patches and plumes is also discussed in (*23*), where a plan-based policy is learned, tested, and evaluated using simulated patches of Chla and then sampled in 2D in the open ocean. In (*24*) the combined use of satellite measurement, AUV and research vessel data was used to describe advection of phytoplankton cells from open waters transported under the sea-ice in the Arctic linking Chla presence, photosynthesis, and biodiversity. Spatial and temporal de-correlation scales in phytoplankton bloom magnitude are reviewed in (*25*), focusing on the U.S. West Coast. (*26*) gives an overview over different 3D interpolation strategies for oceanic data, with the conclusion that kriging is the preferred method for studying the marine pelagic environment.

Our work presents a practical real-world implementation of a sampling approach for the upper water-column, capable of adapting to distributions in 3D. Such uncertain environments require a trade-off between exploration and exploitation; the proposed method presents a solution by splitting the survey into two dedicated phases within a limited volume, bounding time-variability effects. Under these conditions the AUV can map the region of interest in the water-column in an efficient quasi-synoptic manner. We demonstrate the method in a field experiment together with a ship, showcasing the potential of collaborative mapping of planktonic distributions in a dynamic coastal environment.

Sampling Chlorophyll *a* in the Water-Column

Planktonic patchiness can be a result of complex interplay of physical (stirring and mixing), chemical (nutrient availability, CO_2, O_2, and trace metals), and biological (growth, movement, and mortality) processes, which can rapidly change in marine ecosystems and vary across multiple spatio-temporal scales (*27*). These interacting processes create a broad spectrum of patchiness, which can occur in small vertical layers (sub-surface Chla maximum layers [SCML]) (*28*), or in bigger plumes (*29, 30*) which can only be partially visible in remote sensing imagery (Fig. 1). Phenomena such as eddies can interrupt these layers by upwelling or downwelling and potentially create deep Chla maxima layers (DCMs) (*31*). Details about the difference between SCMLs and DCMs can be found in (*32*).

Knowing *where and when* to sample is vital in order to accurately resolve the processes. Furthermore, data collection will, in some cases (especially Lagrangian buoys and floats), itself be influenced by the same forces, such as currents and winds, in addition to the physical limitations of the platform (speed, battery, depth rating, etc.) affecting the spatio-temporal coverage. Capturing synoptic information is therefore a major challenge. Remote sensing data can only obtain coverage at the very surface, omitting valuable information in the depth dimension, and consequently features like the SCM. Furthermore, remote sensing products rarely reach the sub-kilometer resolution, which is vital for evaluation of oceanographic phenomena that control coastal primary productivity at fine scales (*33*).

Chlorophyll *a* Patchiness, Distributions and Interpretation

The advent of fluorometry as a proxy for measuring Chla fluorescence, in addition to the progress of remote sensing approaches, has provided a significant advance in the study of plankton distributions (*34, 35*) providing continuous measurements, where Chla is used as a "common currency" for biomass estimation. Biomass is a broad and practical term used to describe the amount of living material in the water-column. We use the concentration of Chla as an *indicator* of the phytoplankton biomass (organic carbon, expressed as $[mg/m^3]$); hence the terms [Chla] and phytoplankton biomass, or just biomass, is used interchangeably in this text. Although Chla is used as an indicator of phytoplankton biomass worldwide, variability of cellular Chla content is expected to occur as a function of light intensity, species composition and nutrient availability (*36, 37*).

The use of Chla fluorescence measured *in-vivo*, i.e. in live cells measured *in-situ*, as a proxy of phytoplankton biomass and patchiness, needs to be interpreted carefully. When phytoplankton cells are exposed to high light levels for instance (those usually found at the surface ocean, particularly near mid-day during summer) some of the excess of energy absorbed is dissipated as heat (*38*). Part of this is related to a photoprotective process, called *non-photochemical quenching*, that occurs as a rapid response to high light and results in the reduction of fluores-

cence emission at the surface (*39*). Thus, a subsurface Chla fluorescence maximum observed in a vertical profile may not necessarily reflect biomass accumulation, rather, it can be a spurious representation of patchiness. To circumvent this challenge, we compared *in-vivo* fluorescence Chla collected *in-situ* from the AUVs and FRRf measurements, with *in-vitro* Chla, which is derived from filtered water samples and methanol extraction to check whether a subsurface Chla maximum is present at the sampled locations.

At first glance, the complex spatial structure of the phytoplankton distribution occurs as a result of biological and physical processes and interactions in the water-column. The spatial distribution of phytoplankton biomass, its intensity, morphology, and scale dependence (such as the open ocean (10 km–100 km, mesoscale) or coastal zones (10 m–1 km, sub-mesoscale)) is substantially driven by processes, such as turbulent advection, upwelling, convergence, and vertical mixing (*27, 40*). For example, local processes such as upwelling zones can bring deep water nutrients to the surface layer and nurture phytoplankton creating regional hot spots (with high biomass concentration), at scales ranging from 5–10 km (*41*) or even $\leq$ 1 km for complex coastal zones (*42*). In the open ocean, the same aggregation can range from 70–140 km (spatial correlation) in the horizontal plane; while vertically, persistent upper water-column stratification may lead to a subsurface maxima, where phytoplankton is concentrated in the bottom of the pycnocline (density gradient) to better utilize light and nutrients (*43*). Vertical correlation is much weaker due to stratification effects (*26*). Fig. 1b shows the surface distribution of [Chla] for the 2^{nd} of May 2017 along the Norwegian coast, depicting the spatial patterns at the mesoscale.

Regardless of the physical processes taking place, spatial heterogeneity must be "seeded" from external factors that trigger phytoplankton growth, such as nutrient availability and light levels (*4*), in addition to intrinsic evolutionary and physiological traits of the species (e.g buoyancy, vertical migration, and daily cycles of photosynthesis) (*3*), reinforcing the role of physiology on shaping phytoplankton patchiness. Many fluorometers (such as Pulse Amplitude Modulated (PAM) and FRRf) offer the opportunity to study the health of phytoplankton communities, which allow examination of the physiological state of a community and, when combined with reconstructions from AUV surveys, are powerful assets to investigate the spatial structure of phytoplankton distributions (*24*).

Zooplankton grazing is another biological process that accounts for patchiness as it relates to phytoplankton mortality. Although extremely important, it is more difficult to study the effect of such grazing on patchiness due to the non-linear nature of biological interactions and the scarcity of observations that constrain models (*4*). Like phytoplankton, zooplankton themselves are patchily distributed, occurring either in swarms or vertically migrating in the water-column, which complicates the interpretation of abundance due to *under-sampling* – that is being below the *Nyquist sampling rate*, which entails that the dynamics of a phenomena is *not* captured at a level necessary for reconstructing the original distribution (aliasing). The development of acoustic sensors like ADCP (Acoustic Doppler Velocity Profiler), Acoustic Zooplankton Fish Profiler (AZFP), and particle counters capable of collecting continuous zooplankton counts,

provides an opportunity to assess abundance and the phytoplankton influence.

Experimental setting

Our study site is set in the coastal zone of the southern Norwegian Sea. In this region the Norwegian Atlantic Current approaches the coast bringing saline Atlantic water onto the narrow continental shelf (*44*). The Norwegian Coastal Current, carrying freshwater from the outflow of the Baltic and receiving additional freshwater from land run-off as it flows northward along the coast, also enters the shelf in the Møre region (*44, 45*). Both the volume transport of the Norwegian Coastal Current and the lateral location of the interface between Atlantic and coastal water vary seasonally and are strongly affected by wind (*46, 47*); there is also considerable mesoscale variability in the coastal current system (*47, 48*). Mesoscale eddies play an essential role in ocean dynamics, and significantly affect ocean biology and biogeochemistry (*49*). While mesoscale eddies, on scales of a few kilometers to a few hundred kilometres, are known to have a strong effect on plankton distributions, community structure, and diversity (*49*), smaller instabilities can locally enhance vertical mixing (*50*). Such submesoscale processes, on spatial scales of 0.1 to 10 km, can enhance both phytoplankton productivity and its variance on timescales of a few days (*50*).

Repeated sampled temperature and salinity profiles from Skinnbrokleia (7 km south-east of our AUV surveys), were used to place the AUV observations in a local and seasonal setting. Meteorological and oceanographic (met-ocean) time series were from a stationary buoy at Breisundet (14 km north-east of the AUV surveys) were also used. The buoy, placed in 345 m water depth in an inlet between two islands, measures surface waves, wind, current velocity, salinity and temperature at selected depths.

In the weeks preceding the field campaign, the hydrographic conditions in the study area were typical of early summer (*51, 52*). Upper layer salinity was low, and a shallow seasonal thermocline had formed in the upper 10 m (seen in data from a monitoring station on June 8th, 16 km south-east from the survey site). The beginning of the cruise, however, coincided with the onset of stronger winds, around 10 m/s with gusts up to 16 m/s, that prevailed throughout the first half of that week (Fig. 2b). The fresh breeze was accompanied by increasing wave height, up to 2 m (as measured at a stationary met-ocean buoy in Breisundet, 14 km north-east of our AUV and ship observations). Wind stirring during this event caused a deepening of the mixed layer. Time series of temperature and salinity from the met-ocean buoy reveal that the mixing started immediately with the onset of stronger winds on June 17th and progressed during the following days until eventually, temperature and salinity were homogenized down to the 40 m depth level (Fig. 2a).

The AUV and ship-based CTD profiles taken on the same day show a 30 m deep well-mixed layer (Fig. 3). The water-column structure was similar in the AUV survey area and at the ship-based CTD stations some 400 m away. Only in the thermocline between 30 and 40 m depth were

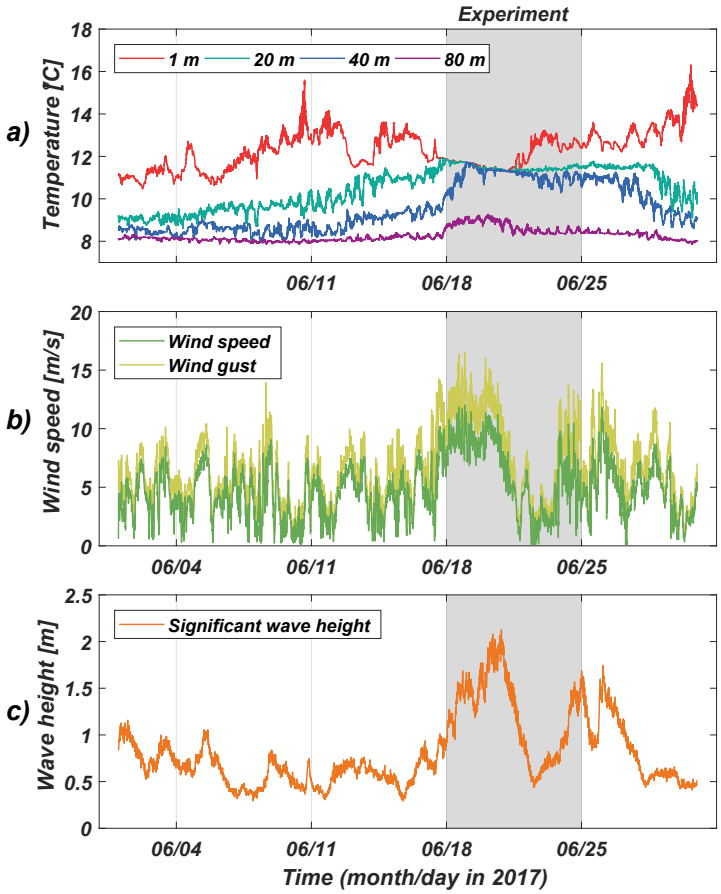

Figure 2: Time series of (a) water temperature at four different depths, (b) wind speed and wind gust, and (c) significant wave height, measured at a buoy located some 14 km inshore of the AUV survey area. The entire month of June 2017 is shown above, with the grey background marking the period of AUV and ship measurements.

some features that were found to be different, such as local temperature inversions, that were seen at one site (CTD stations) but not at the other (AUV survey). The different measurement methods lead to small variations between the profiles: the AUV captured the surface layer from the top centimeter down, while the CTD profile excluded the uppermost meter. On the other hand, the CTD profiles reached deeper than the AUV's maximum dive depth of 50 m. The many profiles from the AUV survey form an envelope that indicates the small-scale spatial variability of temperature and salinity. The difference in water mass properties between the CTD sites and the AUV survey is comparable to the variability within the AUV survey area, which in-turn is comparable in size to the distance between CTD stations and the AUV survey (Fig. 1a).

Gaussian Process Model of the Distribution of Chlorophyll *a*

We use a spatial statistical model, in the form of a Gaussian Process (GP) to model the subsurface Chla maxima (SCM). The GP formulation is widely used for dealing with spatial applications in the ocean (*22, 53*). Its popularity is largely due to the simple yet flexible modeling formulation, which allows consistent and efficient data conditioning. In contrast to a full numerical ocean model, a GP can operate with limited computational resources onboard an AUV and assimilate measurements on the fly.

Measurements were coherently assimilated, to render a more detailed representation of the SCM as the survey progressed. The SCM is predicted by a GP in three dimensional space (latitude, longitude, and depth), by assimilating the identified SCM depth into a 2D grid, of which the detailed steps are explained in the Materials and Methods section. For environmental applications a GP is typically discretized to a grid map with a certain resolution describing variation in space. This map is in essence a collection of random variables (on the grid) with a *multivariate normal probability density function*, where the spatial dependence is captured by a covariance model.

The stochastic process $\{x(s),\ s \in \Omega\}$, with Ω being an indexed grid set $\Omega \subset \mathbb{R}^3$, is a *Gaussian Process* if, for any finite choice of n distinct locations $\boldsymbol{s}_1 \ldots, \boldsymbol{s}_n \in \Omega$, the random vector $\boldsymbol{x} = \big[x(\boldsymbol{s}_1), \ldots, x(\boldsymbol{s}_n)\big]$ has a multivariate normal probability density function:

$$p(\boldsymbol{x}) = N(\boldsymbol{\mu}, \boldsymbol{\Sigma}) = \frac{1}{(2\pi)^{\frac{n}{2}}|\boldsymbol{\Sigma}|^{\frac{1}{2}}} e^{-\frac{1}{2}(\boldsymbol{x}-\boldsymbol{\mu})^T \boldsymbol{\Sigma}^{-1}(\boldsymbol{x}-\boldsymbol{\mu})}, \tag{1}$$

defined by the mean vector $\boldsymbol{\mu} = E(\boldsymbol{x})$, and the symmetric positive definite covariance matrix $\boldsymbol{\Sigma} = \mathrm{cov}(\boldsymbol{x}, \boldsymbol{x})$. The prior mean $\boldsymbol{\mu} = [\mu_1, ..., \mu_n]$ constitutes a 3D surface (latitude, longitude, depth) of the estimated peak Chla layers. The covariance matrix $\boldsymbol{\Sigma}$ is given as:

$$\boldsymbol{\Sigma} = \begin{bmatrix} \Sigma_{11} & \Sigma_{12} & \ldots & \Sigma_{1n} \\ \Sigma_{21} & \Sigma_{22} & \ldots & \Sigma_{2n} \\ \vdots & \vdots & \ddots & \vdots \\ \Sigma_{n1} & \Sigma_{n2} & \ldots & \Sigma_{nn} \end{bmatrix},$$

where, $\Sigma_{ij} = \sigma^2 \mathcal{K}(i,j)$. The stationary covariance has entries depending on the pairwise distance between grid locations. The kernel is defined as:

$$\mathcal{K}(i,j) = (1 + \phi h_{ij}) e^{-\phi h_{ij}},$$

with distance $h_{ij} = |\boldsymbol{s}_i - \boldsymbol{s}_j|$ and ϕ a model parameter indicative of the correlation range (*54*). Capturing the correct spatial correlation is important, as this will affect how the measurements are interpolated. In our experiments, the effective correlation range was set to $\phi \sim 1000$ m based on the East-West variogram results from (*42*) investigating the Chla scale-dependency

for coastal zones using high resolution remote sensing (notably, this implies having correlation across the *smallest* survey area ($\sqrt{700^2 + 700^2} = 990$ m). Here, both larger (*26*) and smaller (*55*) correlation ranges can be defined, depending on the scale of heterogeneity, type of marine system being studied, and prior insight of the water body and ambient conditions.

As measurements are assimilated, the 3D mean surface is adjusted towards the derived Chla maximum depth, and prediction variances are reduced (details are provided in the Materials and Methods section). The SCM peak depth is found for each vertical crossing as the AUV undulates via a 'yo-yo' maneuver in the water-column, where d_t is the AUV location at time t with the corresponding SCM peak (Fig. 8). The measurement model for time t is given by:

$$\boldsymbol{y}_{t,d_t} = \boldsymbol{G}_{t,d_t}\boldsymbol{x} + \boldsymbol{v}_t, \tag{2}$$

where $\boldsymbol{y}_{t,d_t}$ is a length m_{t,d_t} vector of the survey line observation, and the $m_{t,d_t} \times n$ matrix $\boldsymbol{G}_{t,d_t}$ contains '1' entries only at the designated d_t indices, and 0 otherwise. The error term $\boldsymbol{v}_t \sim \mathcal{N}(0, \boldsymbol{R}_{t,d_t})$ represents measurement noise. The covariance matrix $\boldsymbol{R}_{t,d_t}$ is set to a constant diagonal matrix (*56*), and there is no dependence of measurement error terms over assimilation time.

Under Gaussian linear modeling assumptions, the sequential updating of survey data leads to the Gaussian conditional distribution $p(\boldsymbol{x}|\boldsymbol{y}_{1,\boldsymbol{d}_1}, \ldots, \boldsymbol{y}_{t,\boldsymbol{d}_t})$, defined by conditional mean $\boldsymbol{m}_{t,d_t}$ and covariance $\boldsymbol{P}_{t,d_t}$. These equations are recursive over the data gathering steps:

$$\begin{aligned}
\boldsymbol{S}_{t,\boldsymbol{d}_t} &= \boldsymbol{G}_{t,d_t}\boldsymbol{P}_{t-1,\boldsymbol{d}_{t-1}}\boldsymbol{G}_{t,d_t}^t + \boldsymbol{R}_{t,d_t} \\
\boldsymbol{K}_{t,\boldsymbol{d}_t} &= \boldsymbol{P}_{t-1,\boldsymbol{d}_{t-1}}\boldsymbol{G}_{t,d_t}^t\boldsymbol{S}_{t,\boldsymbol{d}_t}^{-1} \\
\boldsymbol{m}_{t,\boldsymbol{d}_t} &= \boldsymbol{m}_{t-1,\boldsymbol{d}_{t-1}} + \boldsymbol{K}_{t,\boldsymbol{d}_t}(\boldsymbol{y}_{t,d_t} - \boldsymbol{G}_{t,d_t}\boldsymbol{m}_{t-1,\boldsymbol{d}_{t-1}}) \\
\boldsymbol{P}_{t,\boldsymbol{d}_t} &= \boldsymbol{P}_{t-1,\boldsymbol{d}_{t-1}} - \boldsymbol{K}_{t,\boldsymbol{d}_t}\boldsymbol{G}_{t,d_t}\boldsymbol{P}_{t-1,\boldsymbol{d}_{t-1}},
\end{aligned} \tag{3}$$

where the mean and covariance matrix are initialized by $\boldsymbol{m}_{0,\boldsymbol{d}_0} = \boldsymbol{\mu}$ and $\boldsymbol{P}_{0,\boldsymbol{d}_0} = \boldsymbol{\Sigma}$.

Results

Experimental setup

The AUV platform used in our experiments was an OceanScan Light AUV (LAUV) (*57*), capable of upwards of 24 hour in-water operation, see Fig. S.1. A Wetlabs EcoPuck was the main sensor payload measuring Chla concentration (470 nm excitation and 695 nm emission peak of Chla) with supplementary sensors including cDOM (color Dissolved Organic Matter), and TSM (Total Suspended Matter), a 16 Hz Seabird Fastcat 49 pumping CTD (conductivity,

temperature, and depth) and an Aanderaa 4831 oxygen optode. The Chla tracking algorithm was hosted on a multicore GPU NVIDIA Jetson TX1 single board computer.

Alongside AUV measurements, both FRRf and two `SilCam` camera systems were used to resolve details of the water-column, as well as allowing cross-reference and verification of AUV measurements and behavior in addition to the algorithm embedded onboard. These systems were deployed from a winch, together with a CTD. The FRRf measures irradiance and [Chla], in addition to photophysiological parameters of the phytoplankton community. The `SilCam` systems imaged a particle size range spanning 28 μm to 4 cm in equivalent diameter, enabling characterization of particle size over a range covering three orders of magnitude in diameter. For accurate fluorescence-based Chla determination and calibration of the FRRf, water samples were collected every 10 m in the upper 60 m on the upward CTD casts using 5-liter Niskin bottles mounted on a rosette frame. Water samples were immediately filtered onto 25 mm glass fibre filters (from GF/F Whatman Inc., Clifton, New Jersey) and stored in a -20°C freezer until analyses in the laboratory, one month later. [Chla] was extracted in 100% methanol for approximately 4 hours at 10°C and fluorometrically determined using a Turner Designs fluorometer. This sampling activity was conducted from the research vessel R/V *Gunnerus*. The survey map and sampling stations are shown in Fig. 1a.

AUV Surveys

The adaptive AUV surveys took ~ 1.5 hrs to complete (Survey 2 covered a larger volume), with a mean vehicle speed of 1.6 m/s over ground; details are provided in Table 1. To follow the GPs model estimate of the SCM 3D surface, two strategies were explored: i) using *fixed* depth (`MODE 1.fixed`) and ii) using an *undulating/yo-yo* motion, ± 2.5 m across the 3D surface (`MODE 2.undulating`). Although finer discretization is possible, given the uncertainty due to current speed and direction, as well as natural stratification, the SCM depth estimates from the GP surface (~ 23 m resolution) were discretized into 200 m segments for the AUV to follow.

Survey	**Time and Date**	**Duration**	**Mean Vel.**	**Area**	**Mode**
1	20.06.17-10.02 AM	1h 33min	1.5 m/s	700 m^2	Fixed depth
2	20.06.17-12.10 AM	1h 58min	1.5 m/s	900 m^2	Fixed depth
3	22.06.17-11.06 AM	1h 27min	1.6 m/s	700 m^2	Undulating ± 2.5 m

Table 1: AUV survey information and details.

A detailed analysis of the approach is presented focusing on Survey 1, using *fixed* depth control and comparing that with Survey 3, tracking the 3D surface using an *undulating/yo-yo* pattern. Results from Survey 2 are shown in Fig. S.3.

In Fig. 3b, the first ~ 4 km is used to cover the sides of the volume (`MODE 1`), gathering an estimate of the SCM, before `MODE 2` tracks this estimate by either *fixed* or *undulating/yo-yo*

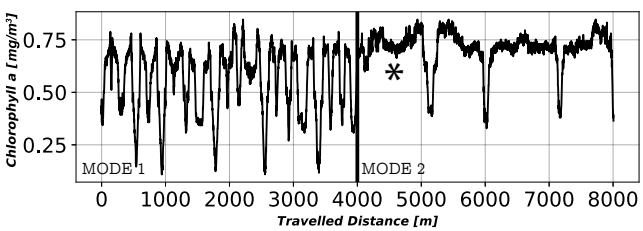

(a) Chla consentration vs. travelled distance.

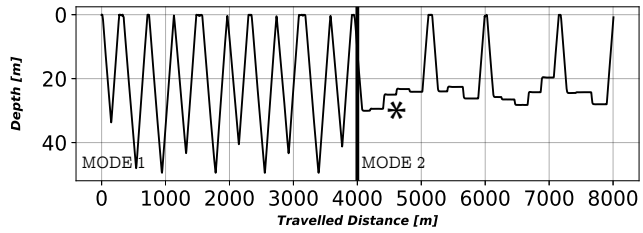

(b) Depth vs. travelled distance.

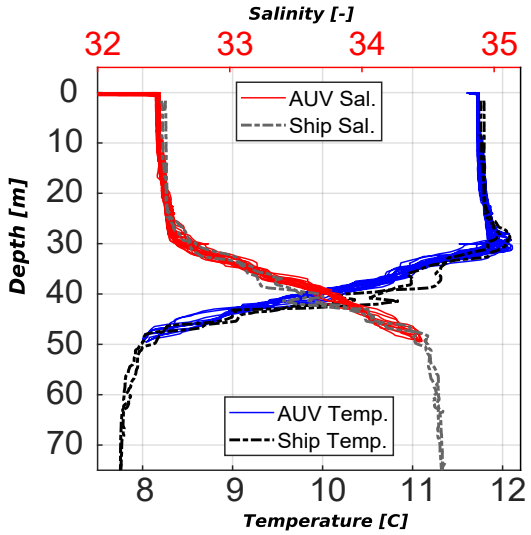

(c) Temperature and salinity.

Figure 3: Data from Survey 1 (`MODE 1.fixed`) using *fixed* tracking of the 3D Chla surface. The * marks a point where the AUV behavior transitions, as the depth adjustment is followed by increased [Chla] also shown in Fig. 4. (a) The Chla concentration vs. travelled distance accumulated over ground. (b) Temperature and salinity curves from AUV and the *R/V Gunnerus* from the same area. (c) AUV depth vs. travelled distance. Note the adjustment of survey depth as the AUV is following the 3D surface (in 200m increments).

behavior. `MODE 2`, in turn, trails an hourglass pattern in the interior of the volume for the next $\sim$ 4 km (see Materials and Methods for more details). The second half of Fig. 3b shows the AUV adjusting its depth according to the SCM estimate, with periodic surfacing events when reaching the corner points of the survey box. Both Survey 1 (Fig. 3a) and Survey 3 (Fig. 5a) confirm that the [Chla] concentrations are higher during the tracking phase of `MODE 2`, with the AUV sampling between the 20-30 m depth range. These depths correspond to the SCM found from analysis of the water samples taken from the research vessel and shown together in Fig. 6 with FRRf data. The temperature and salinity data in Fig. 3c suggest that the water-column was well mixed down to 30 m, where an abrupt gradient is present. This interface influences the distribution of biomass in the water-column (*58*).

Since the first phase (`MODE 1`) took $\sim$40 minutes to complete, some of the estimates are likely impacted by current velocity and direction. It is therefore important to verify that the depth adjustments result in an increase of [Chla]. Elevated levels of [Chla] can be seen throughout the second phase of the missions, but to verify this further, both Fig. 3a, 3b, and 4b and 4c have been marked with an asterisk (*) that show the first part of the SCM tracking, and how the depth adjustment successfully results in elevated levels of [Chla]. The first part is chosen, as the earliest observations have the highest probability of being affected, due to their high lag

between the initial measurements and re-visitation, impacted by current.

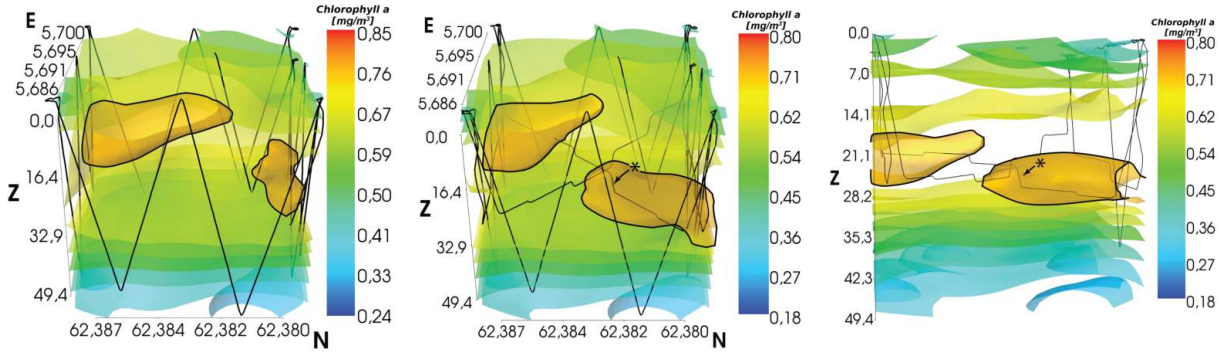

(a) Volumetric estimate after `MODE 1`

(b) Volumetric estimate after `MODE 2`

(c) Volumetric estimate after `MODE 2` (side view)

Figure 4: (a) Volumetric representation (3D kriging) of the [Chla] iso-surfaces *after the initial survey phase* (`MODE 1`) covering the sides of the volume. The AUV path is overlaid (black line) and N, E, Z are labels for North, East, and Depth. (b) The volume *after the adaptive survey of the internal volume* (`MODE 2`), rendering more of the internal [Chla] structure. Notice the depth adjustment (marked *) in the interior that is making the AUV stay in the region of high concentration. (c) Side view of the same volume as in b), to highlight the adaptive depth adjustments performed by the AUV. The color scale of the interior iso-surfaces is affected by the transparency. Plots constructed in *Mayavi* (*59*).

Furthermore, by comparing the volumetric estimate before (Fig. 4a) and after (Fig. 4b and 4c) the interior survey, we can see the distribution change in light of the new measurements. The iso-surfaces (marked with black lines in Fig. 4) change, resolving the interior information with finer detail. The change is greatest within the volume, which is expected, as these are unsurveyed locations, previously estimated based on the data from the sides. It is still evident, that the main features and distribution is largely similar before and after the initial survey. This coherence both supports the credibility of the design premise, limiting the survey size to effectively handle time dynamics, as well as the shared information between the interior and boundary used to focus sampling.

Comparing the results to Survey 3 using the *undulating/yo-yo* depth tracking, shows that Survey 3 also has elevated concentrations while tracking the SCM. As the *undulating/yo-yo* approach is less sensitive to errors in the depth estimate while providing higher sampling density at the SCM, it is more practical for mapping the structure of the SCM, but only subject to a certain current regime; with strong currents, a *fixed* depth approach would likely be preferable because of shorter survey times.

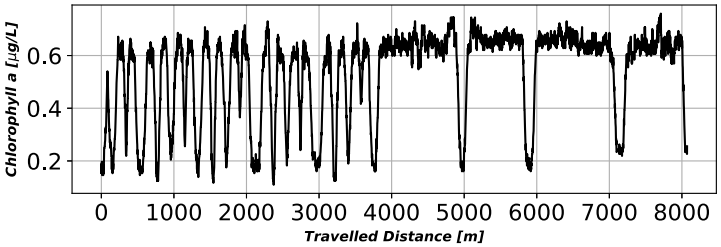

(a) Chla consentration vs. travelled distance.

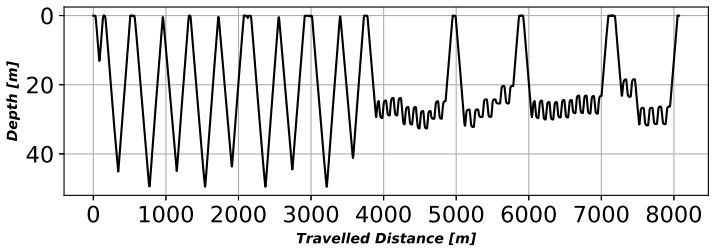

(b) Depth vs. travelled distance.

Figure 5: Survey 3 using undulating tracking control during the survey. (a) The [Chla] vs. travelled distance accumulated over ground. (b) AUV depth vs. travelled distance.

FRRf Measurements

Name	**Area**	**Tide**
Station 1 - 19.06.17 - 10.15 AM	Survey 2	Ebb
Station 2 - 19.06.17 - 13.55 AM	Survey 2	Low
Station 3 - 19.06.17 - 16.15 AM	Between S2 & S1	Rise
Station 4 - 20.06.17 - 10.30 AM	Survey 1	Ebb
Station 5 - 20.06.17 - 13.05 AM	Survey 1	Low
Station 6 - 21.06.17 - 10.10 AM	West of S1	High
Station 7 - 21.06.17 - 14.45 AM	West and between S2 & S1	Low

Table 2: FRRf survey data gathered from Stations 1-7, shown in Fig. 1a.

Fig. 6 shows a vertical profile of the *in-vitro* (extracted) and the *in-vivo* (measured *in-situ*) [Chla] derived from the FRRf deployed at Stations 4 and 5 and from AUV Survey 1 indicated on the map in Fig. 1a. Details on inter-calibration can be found in (*24*). In the *in-situ* assessments (FRRf and AUV), [Chla] is higher (> 0.6 mg m^{-3}) at the upper 30m, decreasing gradually below this depth (< 0.8 mg m^{-3}). The vertical structure of [Chla] is in agreement with salinity profiles, confirming that the depth of the mixed layer approaches 30m. At Stations 4 and 5, the *in-situ* observations (from the FRRf) agreed with the results from the *in-vitro* [Chla]. Both measurements reveal a similar vertical pattern, such as a subsurface maximum (from 10 to 25

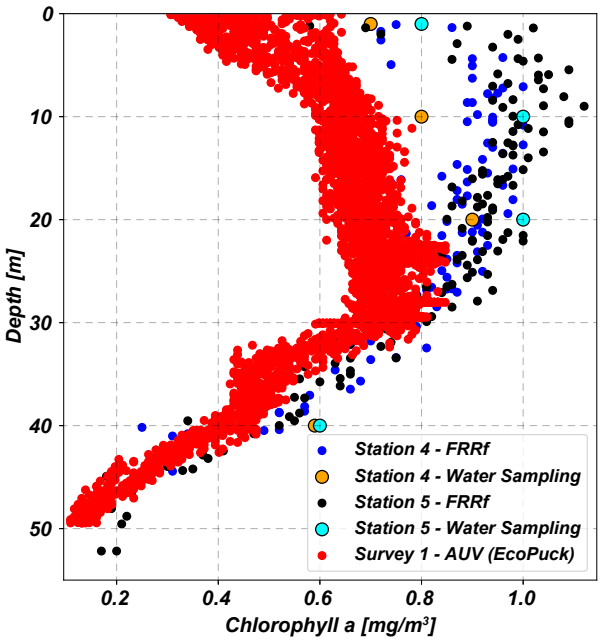

Figure 6: Comparisons of *in-situ* [Chla] derived from the AUV (EcoPuck) and FRRf profiling measurements, as well as *in- vitro* [Chla] extracted from water samples. The differences in [Chla] at the surface between the two sensors is due to the hydrography of the two stations despite proximity.

m), suggesting a higher concentration of phytoplankton cells at this depth, although this trend is much less pronounced than for the AUV data. When compared to the AUV Survey 1, [Chla] varies slightly in the upper 30m (a difference of 0.2 mg m^{-3} of [Chla]), which could imply that the hydrography was different between Stations 4 and 5 and Survey 1, despite the proximity of sites. This result reemphasizes the need for using robotic sampling to monitor the variability and patchiness of phytoplankton distributions.

A quenching (reduction) of the fluorescence signal in live cells (*in-situ*) is commonly found in surface waters during summer, when phytoplankton are exposed to high light levels. This occurs to protect the cells' photosystems (a process called non-photochemical quenching [NPQ] (*38*)), by converting part of the excess energy to heat. Results from this study show that the *in-vitro* [Chla] presented approximately the same vertical pattern as the *in-situ* measurements, with a subsurface maximum at 20 - 30 m depth. This suggests that NPQ processes were not evident in this study, possibly because of cloudy conditions. Clouds reduce the amount of light that reaches the surface water and, consequently, such conditions do not interfere as much with the *in-situ* fluorescence measurements derived from the sensors.

`SilCam` Observations

While *in-situ* [Chla] derived from the FRRf and the AUV provided relevant information regarding phytoplankton patchiness, there may exist some linkages to biological activity (e.g. grazing) at higher trophic levels, and thus, larger particle sizes. Results from the two `SilCam` particle imaging systems provided *in-situ* images of suspended material allowing insight into the presence and distribution of larger phytoplankton and zooplankton, in addition to other material in the water-column, such as marine snow and suspended sediments.

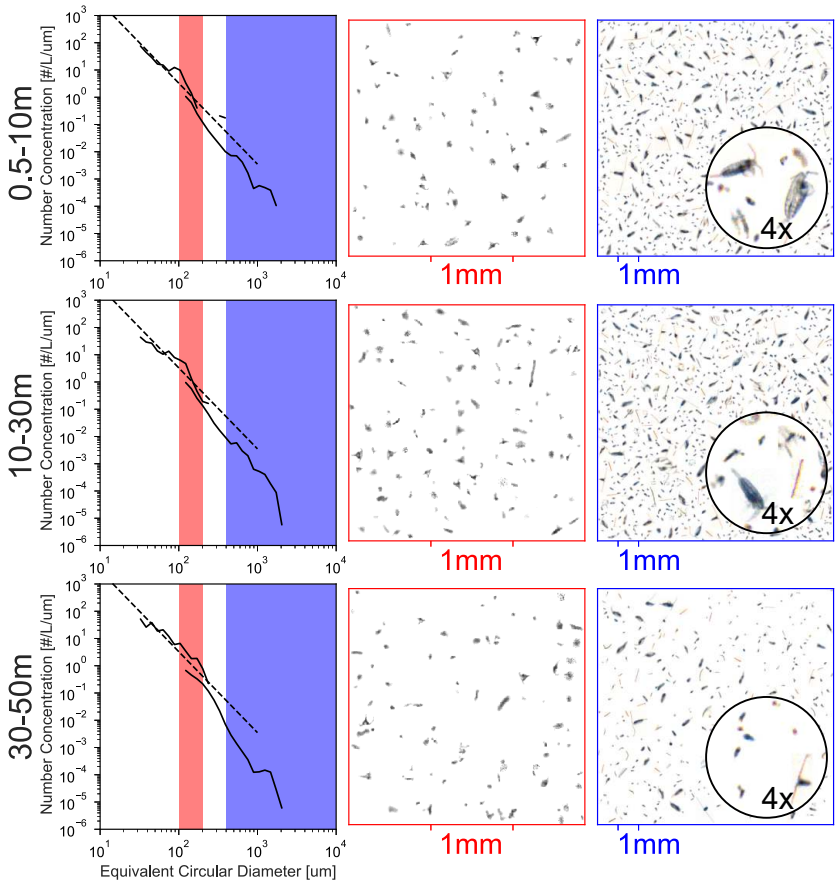

Figure 7: Sample imaging information from the `SilCam` obtained at Station 4 and 5. Data presented are averaged from both stations, and discretized into three depth ranges from 0.5-10 m (top row), 10-30 m (middle row) and 30-50 m (bottom row). The left column shows the particle number distribution from the two magnifications of `SilCam` that were deployed, with the montages of particles from the *red shaded region* presented in the images in the middle column of the figure, and *the blue shaded region* in the images in the right column of the figure. The dashed line in the particle number distributions represents the average fitted Junge distribution (*60*) (between 100-300 μm) from all depths.

Fig. 7 shows particle number distribution and sample images recorded within the diameter range of 30-10000 μm at Station 4 and 5 using the two `SilCam`'s with different magnifications. With an average exponent (m) of 3 (shown by the dashed lines in Fig. 7), the size distribution follows approximately that of a Junge distribution (*60*):

$$n(D) = kD^{-m} \tag{4}$$

where $n(D)$ is the number of particles of diameter D; k is a constant that scales according to the particle concentration; m is the slope of the distribution. In the simplest form, the Junge distribution is an approximation of the particle size distribution, made up of a series of multiple log-normal distributions with varying median sizes that arise from sub-populations of particulate material such as specific types of phytoplankton, zooplankton or marine snow (*61*). In Fig. 7, the observed distributions show many points of variation from this average Junge slope, with one peak at just over 100 μm that corresponds to a high abundance of the dinoflagellate genus *Ceratium* (indicated by the red shaded region), which can be seen in the middle column of the figure. The copepod genus *Calanus* are also highly abundant (indicated by the blue shaded region), and can be seen in the right-most column of the figure. In the montages of particle images (right two columns of Fig. 7), individual particle images are packaged into the plot by randomly sampling from the recorded size distribution so as to maintain the ratio of large-to-small particles, albeit without being representative of the true concentration of particles, which was more sparse *in-situ*.

Most particulate material is present within the top 10 m, and it is where relative abundance of *Ceratium* appears greatest as the 100 μm peak in the particle number distribution is most prominent. The *Ceratium* is still present in approximately the same concentration between 10-30 m, but is surrounded by a higher concentration of other material also present within this depth range. This is evidenced by the reduced dominance of the 100 μm peak. Below the thermocline at 30 m the *Ceratium* peak in the number distribution is not discernible and there is less total material in suspension. With such a high dominance of biological material in the water, the reduced concentrations below 30 m, observed by the `SilCam`, agree well with the reduced [Chla]. The highest load of particulates observed by particle imaging was within the 10-30 m depth range, which also corresponds to the SCM. However, the small difference in the concentration of material at 100 μm between the 0.5-10 m and 10-30 m depth ranges suggests that other smaller phytoplankton species (possibly not captured by the imaging system), in addition to *Ceratium*, are contributing to the SCM.

Discussion and Conclusion

We have presented methods for autonomously mapping spatial heterogeneity of phytoplankton biomass in 3D using AUVs, by combining GP models and robotic sampling. The method

is shown to successfully estimate and track layers of high Chla concentration, focusing sampling efforts and increasing resolution along important features such as the SCM. We use spatial modeling and interpolation to reconstruct the distribution in 3D. This volumetric estimate is then augmented with *in-situ* images of suspended particles, fluorometry and discrete water samples, taken co-temporally from a research vessel. Comparison of in-field data shows correspondence between AUV data and behavior, providing a broad and extensive perspective of the pelagic activity. The results demonstrate the complexity of conducting interdisciplinary coastal ecology, and why unification of marine data sources is necessary towards achieving a detailed environmental picture of the water-column.

Limitations and Future Steps

The largest source of sampling uncertainty comes from the effects of currents (speed and direction), making the observations time-dependent. The AUV used in this study is fast enough to discover and make use of spatial structure, but not so fast as that it can capture the full spatial field at any time, since an AUV is not a *synoptic* measurement platform. Ideally, the AUV should therefore try to "stay" with the same water mass, working in a Lagrangian frame of reference to reduce these effects. Lagrangian correction is however non-trivial and unless a good proxy measurement of advection can be provided (such as from a surface drifter), there is limited value in adding to experimental complexity (see (*22*) for a more detailed discussion). This is even more difficult to capture within a 3D volume, or within the coastal zone, in waters such as off of Runde. A simple and effective measure to account for this is to limit the method/survey area to sub-kilometer size, setting a bound on these uncertainties similar to the *enclosure criterion* used in (*9*). Using this strategy, allows us to use directed Euclidean sampling of the interior volume, while increasing sampling resolution and determining SCM variability. This can be seen by looking at the recorded data and comparing the estimated Chla distribution before and after the initial survey as in Fig. 4 where only a minor current influence was discernable (except at unobserved locations).

Furthermore, the approach is designed with two modes, `MODE 1` that is purely exploratory and `MODE 2` that is exploitative. Consequently, the most interesting part of the volume is surveyed last. This is important since prior data from `MODE 1` allows sampling (the interior) to proceed with higher survey speed and reduced probability of losing track of the feature. The number of 'yo-yo' envelopes is platform dependent and the spacing, depth, and number of envelopes could be used to further optimize the time spent finding an adequate estimate. Additionally, forsaking some surfacing events could help reduce survey time, if more accurate navigation is possible. At the cost of a greatly increased operational complexity, additional assets such as another AUV could be used to increase coverage capacity and sampling density, should sharing of information between assets be available (e.g. (*55*)).

The AUV does not update the survey depths based on measurements inside the volume due

to the previously mentioned factors such as "hit-or-miss" consequences, and time-variability effects. Using the measurements from the interior (within the 3D volume) survey can be considered in future work, although the value of this information is limited due to the small survey area and correlation scales present in the coastal ocean. Thus, making use of this data can be challenging. One possible use would, for instance, be to improve the undulating depth from a fixed oscillation to a data adjusted offset. It is also the case, that variability in the ocean is higher along the vertical axis, motivating the use of such capabilities. However, this variability depends on a host of factors, and can be hard to estimate correctly without the aforementioned drawbacks. Furthermore, the results from this work show that platforms like AUVs can make measurements adequate to resolve fine scale features by using an enclosure criteria. This is also apparent in the results presented, which shows a clear spatial coherence throughout the mission (see Fig. 4).

The volumetric results from kriging (such as Fig. 4) are dependent on the accuracy of the correlation parameters used. The values used in this paper are based on the variogram from (*42*) and can only give a suggestive estimate for conducting similar experiments. Aspects of spatial correlation and use of marine sensor fusion towards description of the water-column on the submesoscale require effort which is not within the scope of this work. This includes looking at the time dependence of the data, as well as utilizing previous historical data sources ((*25, 62*)).

Future integration of particle imaging instruments onboard the AUV would greatly change how volumetric surveys can be conducted, both enabling adaptation based on taxonomically descriptive data (targeting harmful algal blooms or other materials such as suspended plastics), as well as reducing the current sensitivity to patchiness arising from ship-based winch deployment.

Materials and Methods

The aim of the approach is to obtain a fine-resolution synoptic view of a water-column feature, using a single AUV, by concentrating sampling efforts in the water-column. In our case, the feature of interest is the subsurface chlorophyll maximum (SCM). To achieve this, sampling is split into two modes or phases – an initial phase dubbed `MODE 1` that is explorative, followed by a second phase (`MODE 2`) that exploits the information from the first phase towards sampling a feature of interest, using the data to plan the survey. By this design the most interesting part of the volume is surveyed last, allowing the time spent mapping it at high resolution to be minimized. This is a subtle, but important point as this both reduces spatial and temporal uncertainty of the most critical measurements. To avoid redundant data collection, sampling of the volume is also split between the modes. `MODE 1` surveys the sides of the volume, while `MODE 2` surveys the interior. `MODE 1` uses a spatial model (GP) to estimate how the SCM is distributed inside the volume, so that `MODE 2` can follow these estimates subsequently. The following and Fig. 8 shows these steps in detail:

Step 1) `MODE 1`
Aim: Estimate the SCM inside the volume using the GP model.
Behavior: Survey the sides (red square shown Fig. 8) of the volume, while doing 'yo-yo' envelopes from 0 to 50 m in depth.
Tasks:

`MODE 1.peak` Identify the depth of the Chla peak.

`MODE 1.assimilate` Assimilate SCM depths into a GP surface.

Step 2) `MODE 2`
Aim: Use the learned information from `MODE 1` to perform a detailed survey.
Behavior: Track the GP SCM depth 3D surface inside the AUV survey volume following an hourglass pattern (shown as blue lines in Fig. 8) chosen to specifically cover as much of the interior in as short a time.
Tasks:

`MODE 2.fixed` - Follow the estimate using *fixed depth* control.

`MODE 2.undulating` - Follow the estimate using *undulating depth* control.

`MODE 1` comprises the initial phase, where the location and depths of the SCM are to be identified and assimilated (`MODE 1.assimilate`) into the GP SCM depth 3D surface. During each full 'yo-yo' envelope (one descent and one ascent) the final SCM depth is to be found and stored as *[latitude, longitude, depth, Chla concentration]*. It is the task of the subroutine `MODE 1.peak` to do this analysis. The function will decide the final SCM depth based on the following logic:

1. Segment the concentration measurements into depth bins with average measurements. Collecting 5 data points in one bin, with an average depth.
2. Find the two depths corresponding to the largest ($depth_1$) and second largest ($depth_2$) concentration spikes.
3. Calculate the depth difference between these spikes.
4. If the depth difference is less than 10 m, the SCM depth is set to the depth of the largest concentration: $SCM_{depth} = depth_1$.
    - If not, the SCM depth is set to a weighted mean, as $SCM_{depth} = depth_1 * 0.70 + depth_2 * 0.30$. This is based on the fact that approximately 70% of normally distributed values are within 1 standard deviation of the mean.

The subsequent subroutine `MODE 1.assimilate` will integrate the final SCM_{depth} into the GP model (Eq. (3)), using the observation location (*lat, lon* $\rightarrow$ *grid cell*), and "lifting" or "lowering" the depth estimate at the surrounding locations/grid cells within the correlation range. These two concepts are encapsulated in Fig. 8.

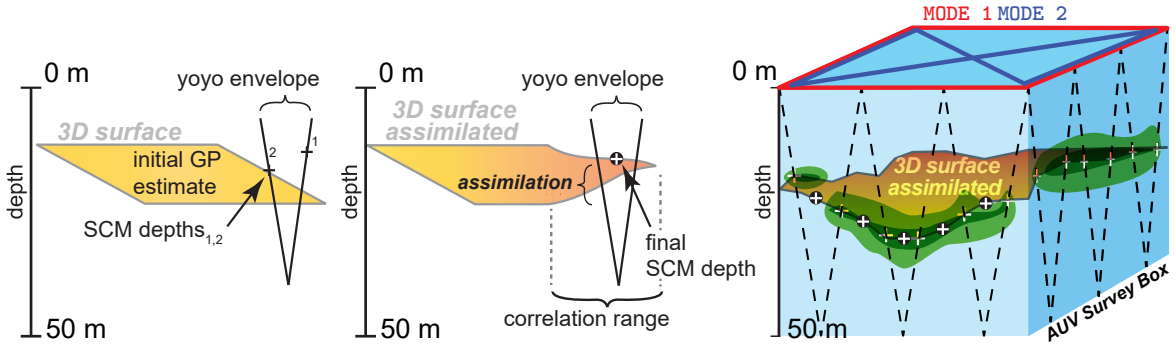

Figure 8: A 3D conceptual view of our approach. After each 'yo-yo' envelope, two SCM peak depths are found and the final SCM is determined. The final SCM depth is then assimilated into the GP model's 3D SCM surface. Left panel: the AUV transects (black dashed line), peak detection (black/white crosses), `MODE 1` (*red lines* [box]), `MODE 2` (*blue lines* [hourglass]), true distribution (green blobs), with the 3D surface of the sub-surface Chla maxima depth shown as the tan surface.

Once the GP SCM depth 3D surface has been established, the AUV switches to `MODE 2` and depth tracking mode where the goal is to provide a high resolution volumetric representation of the Chla structure by tracking this 3D surface either in `MODE 2.fixed` or `MODE 2.undulating` following a 3D path. This enables an effective and improved way of mapping detail within the SCM. The biomass patchiness can thus be evaluated and augmented with supporting ship-based samples, allowing organism community structure to be described more accurately.

Kriging in 3D

Using kriging (*54*), a 3D representation of the volume can be constructed, conditioned on the data. The kriging surface is the interpolated prediction given as the conditional mean of the GP, while providing the conditional prediction covariance in an explicit form.

Spatial correlation is an essential component of kriging, and this is incorporated by a kernel function which relies on the distance between pairs of locations, $h_{ij} = |\boldsymbol{s}_i - \boldsymbol{s}_j|$; in this work this is measured in three-dimensional $[x, y, z]$ coordinates. Compared with the more common 1D or 2D applications of kriging, this means a considerable increase in the size of the covariance matrices required for data conditioning – assimilating all the samples from the survey is

therefore not practical when doing the interpolation. In our approach a pruned version of the assimilated 1700 samples from this volume was used, with a square size 2700 covariance matrix (reflecting the $[30 \times 30 \times 30]$ volume grid).

The interpolation time on a Dell Latitude E7540 i7 took approximately 1.5 minutes with these parameters, resulting in figures such as Fig. 4. To capture the difference between horizontal and vertical correlation distance, the z-dimension is artificially exaggerated by a factor of about 20 based on (*26*). The horizontal correlation was, as previously discussed, based on the East-West variogram from (*42*). While there are methods for handling memory and computational time challenges for 3D GPs, our focus is on an applied study using `MODE 1` to define a region of interest.

Supplementary Materials

Fig. S.1: LAUV Platform.
Fig. S.2: Experiment Overview.
Fig. S.3: Survey 2 Data.

References and Notes

1. P. G. Falkowski, R. T. Barber, V. Smetacek, *Science* **281**, 200 (1998).
2. M. Dowd, E. Jones, J. Parslow, *Environmetrics* **25**, 203 (2014).
3. W. M. Durham, *et al.*, *Nature communications* **4**, 2148 (2013).
4. A. Martin, *Progress in oceanography* **57**, 125 (2003).
5. E. K. Hovland, H. M. Dierssen, A. S. Ferreira, G. Johnsen, *Marine Ecology Progress Series* **484**, 17 (2013).
6. A. Bracco, A. Provenzale, I. Scheuring, *Proceedings of the Royal Society of London B: Biological Sciences* **267**, 1795 (2000).
7. C. Perruche, P. Rivière, P. Pondaven, X. Carton, *Journal of marine systems* **81**, 99 (2010).
8. S. J. Brentnall, K. J. Richards, J. Brindley, E. Murphy, *Journal of Plankton Research* **25**, 121 (2003).
9. J. Das, *et al.*, *The International Journal of Robotics Research* **31**, 626 (2012).

10. E. Davies, P. Brandvik, F. Leirvik, R. Nepstad, *Marine Pollution Bulletin* **115**, 105 (2017).

11. L. Stemmann, E. Boss, *Annual Review of Marine Science* **4**, 263 (2012).

12. Y. C. Agrawal, H. C. Pottsmith, *Marine Geology* **168**, 89 (2000).

13. G. Graham, A. Nimmo-Smith, *Limnology and Oceanography: Methods* pp. 1–15 (2010).

14. H. M. Sosik, R. J. Olson, *Limnology and Oceanography: Methods* **5**, 204 (2007).

15. M. A. Moline, *et al.*, *Journal of Atmospheric and Oceanic Technology* **22**, 1797 (2005).

16. I. Robbins, *et al.*, *Harmful Algae* **5**, 749 (2006).

17. Y. Zhang, *et al.*, *OCEANS 2015 - MTS/IEEE Washington* (2015), pp. 1–5.

18. J. P. Ryan, *et al.*, *Limnology & Oceanography: Methods* **8**, 394 (2010).

19. J. Das, *et al.*, *The International Journal of Robotics Research* **34**, 1435 (2015).

20. R. N. Smith, *et al.*, *OCEANS Conference IEEE Sydney, OCEANSSYD 2010* (2010).

21. R. N. Smith, *et al.*, *Journal of Field Robotics* **28**, 714 (2011).

22. R. Graham, *et al.*, *International Symposium on Experimental Robotics* (Springer, 2013), vol. 88, pp. 819–839.

23. D. Magazzeni, F. Py, M. Fox, D. Long, K. Rajan, *Autonomous Robots* **37**, 47 (2014).

24. G. Johnsen, *et al.*, *Polar Biology* pp. 1–20 (2018).

25. S. Frolov, R. M. Kudela, J. G. Bellingham, *Harmful Algae* **21-22**, 1 (2013).

26. J. Sahlin, M. A. Mostafavi, A. Forest, M. Babin, *Marine geodesy* **37**, 238 (2014).

27. S. Van Gennip, *et al.*, *Journal of Geophysical Research: Oceans* **121**, 4149 (2016).

28. J. J. Cullen, *Annual Review of Marine Science* **7**, 207 (2015).

29. W. M. Durham, R. Stocker, *Annual Review of Marine Science* **4**, 177 (2012).

30. W. O. Smith Jr, D. J. Demaster, *Continental Shelf Research* **16**, 291 (1996).

31. J. Weiss, A. Provenzale, *Transport and Mixing in Geophysical Flows*, Lecture Notes in Physics (Springer Berlin Heidelberg, 2007).

32. A. Morel, J.-F. Berthon, *Limnology and oceanography* **34**, 1545 (1989).

33. V. S. Hemsley, *et al.*, *Environmental science & technology* **49**, 11612 (2015).

34. C. J. Lorenzen, *Deep Sea Research and Oceanographic Abstracts* (Elsevier, 1966), vol. 13, pp. 223–227.

35. R. C. Smith, K. S. Baker, P. Dustan, *SIO Ref* **81**, 17 (1981).

36. J. J. Cullen, *Canadian Journal of Fisheries and Aquatic Sciences* **39**, 791 (1982).

37. M. Felip, J. Catalan, *Journal of Plankton Research* **22**, 91 (2000).

38. J. J. Cullen, J. G. MacIntyre, *Nato ASI Subseries G: Ecological Sciences* **41**, 559 (1998).

39. S. Roy, C. A. Llewellyn, E. S. Egeland, G. Johnsen, *Phytoplankton pigments: characterization, chemotaxonomy and applications in oceanography* (Cambridge University Press, 2011).

40. D. L. Mackas, K. L. Denman, M. R. Abbott, *Bulletin of Marine Science* **37**, 653 (1985).

41. A. P. Martin, K. J. Richards, A. Bracco, A. Provenzale, *Global Biogeochemical Cycles* **16**, 9 (2002).

42. R. D. Hedger, T. J. Malthus, A. M. Folkard, *Remote Sensing of the Ocean and Sea Ice 2002* (International Society for Optics and Photonics, 2003), vol. 4880, pp. 146–158.

43. G. M. Silsbe, S. Y. Malkin, *Aquatic microbial ecology and biogeochemistry: A dual perspective* (Springer, 2016), pp. 141–152.

44. R. Sætre, R. Ljøen, *Proceedings of the First International Conference on Port and Ocean Engineering under Arctic Conditions* (1972), vol. 1, pp. 514–535.

45. O. Pedersen, K. Tande, D. Slagstad, *Deep-Sea Research II* **48**, 567 (2001).

46. R. Sætre, J. Aure, R. Ljøen, *Continental Shelf Research* **8**, 239 (1988).

47. M. Mork, *Phil. Trans. R. Soc. Lond. A* **302**, 635 (1981).

48. J. A. Johannessen, E. Svendsen, S. Sandven, O. M. Johannessen, K. Lygre, *Journal of Physical Oceanography* **19**, 3 (1989).

49. J. D. J. McGillicuddy, *Annual Review of Marine Science* **8**, 13.1 (2016).

50. A. Mahadevan, *Annual Review of Marine Science* **8**, 161 (2016).

51. H. Svendsen, *Ecology of fjords and coastal waters*, H. R. Skjoldal, C. Hopkins, K. E. Erikstad, H. P. Leinaas, eds. (Elsevier Science B.V., 1995).

52. P. Wassmann, H. Svendsen, A. Keck, M. Reigstad, *Journal of Marine Systems* **8**, 53 (1996).

53. J. Binney, A. Krause, G. S. Sukhatme, *The International Journal of Robotics Research* **32**, 873 (2013).

54. N. A. C. Cressie, C. K. Wikle, *Statistics for Spatio-Temporal Data.*, Wiley Series in Probability and Statistics (Wiley, 2011).

55. S. Kemna, *Multi-Robot Strategies for Adaptive Sampling with Autonomous Underwater Vehicles*, PhD thesis, University of Southern California (2018).

56. C. Wunsch, P. Heimbach, *Physica D: Nonlinear Phenomena* **230**, 197 (2007).

57. A. Sousa, *et al.*, *Navigation, Guidance and Control of Underwater Vehicles* (2012), vol. 3, pp. 268–274.

58. L. C. Lund-Hansen, *Hydrobiologia* **673**, 105 (2011).

59. P. Ramachandran, G. Varoquaux, *Computing in Science & Engineering* **13**, 40 (2011).

60. H. Bader, *Journal of Geophysical Research* **75**, 2822 (1970).

61. M. Jonasz, G. Fournier, *Limnology and Oceanography* **41**, 744 (1996).

62. S. Frolov, B. Garau, J. Bellingham, *Journal of Geophysical Research: Oceans* **119**, 5071 (2014).

63. Runde Environmental Centre, Norway, http://rundecentre.no.

64. SINTEF Ocean AS, ENTiCE project webpage, https://sintef.no/prosjekter/entice/.

65. Centre for autonomous marine operations and systems (AMOS), https://ntnu.edu/amos.

Acknowledgements

We are grateful to the resident scientists at the Runde Environmental Centre (*63*), the captain and crew of *Ophelia* and NTNU's research vessel, the R/V *Gunnerus*. The met-ocean buoy data was obtained from the Norwegian Meteorological Institute. The monitoring station data was collected by Roger Kvalsund at the Runde Environmental Centre on commission from the Norwegian Institute for Water Research (NIVA), as part of the *Ecosystem Monitoring of Coastal Waters* programme financed by the Norwegian Environment Agency.

Funding: This work was part of the `ENTiCE` project (*64*) funded by the Research Council of Norway Project # 255303/E40, the Nansen Legacy Program, project number # 27272, and AMOS (*65*), Center of Excellence, project number # 223254.

Author contributions: TF, GF, ED, JU, RM, GJ, IE, JE, ML, and KR contributed to the manuscript. TF and ML performed the field experiments, while GF, ED, and GJ were responsible for `SilCam` and FRRf operations and subsequent data analysis. RM was responsible for remote sensing. Oceanography of the Runde region was articulated by JU and IE.

Competing interests: The authors declare no competing financial interests.

Data and materials availability: All (other) data needed to evaluate the conclusions in the paper are present in the paper or the Supplementary Materials.

Supplementary Materials for

Towards Adaptive Robotic Sampling of Phytoplankton in the Coastal Ocean

Trygve O. Fossum*[,1,10], Glaucia M. Fragoso[2], Emlyn J. Davies[4], Jenny E. Ullgren [7], Renato Mendes [5,6], Geir Johnsen[2,8,10], Ingrid Ellingsen[4], Jo Eidsvik[3], Martin Ludvigsen[1,8,10] and Kanna Rajan[5,9,10].

*Corresponding Author: *trygve.o.fossum@ntnu.no*

August 19, 2019

The PDF file includes:

Figure S.1: LAUV Platform. NTNU's Light AUV platform (*Harald*) for upper water-column exploration used in our work. The onboard EcoPuck sensor ([Chla], [cDOM], and [TSM]) is shown as mounted on the AUV in the upper left corner.

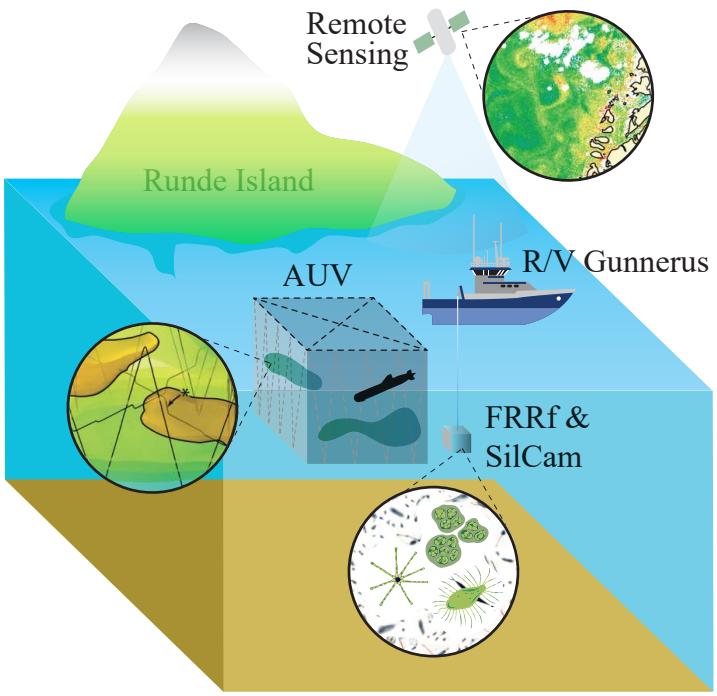

Figure S.2: Experiment Overview. The systems, scales, and platforms used in the field experience: remote sensing (Chlorophyll *a*), AUV (biological and physical measurements), and R/V Gunnerus (FRRf [fluorometry] and SilCam [particle camera]). Focusing in on a volume of water: starting at satellite observation, AUV mapping in 3D, and finally images and measurements of individual particles in the water-column, covering a unique range of scales in the coastal microbial community.

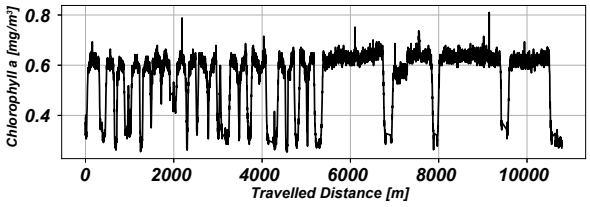

(a) Chla consentration vs. travelled distance.

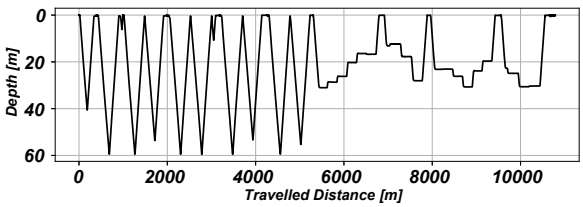

(b) Depth vs. travelled distance.

Figure S.3: Survey 2 Data. Measurements from Survey 2 (20.06.17 at 12.10 AM) over a 900 m^2 area using *fixed* tracking of the 3D Chla surface. Similar to the other surveys the observed [Chla] is higher when tracking the sub-surface Chla maxima. (a) The Chla concentration vs. traveled distance accumulated over ground. (b) AUV depth vs. traveled distance. Note the adjustment of survey depth as the AUV is following the 3D surface (in 200 m increments).